Journal of the European Ceramic Society 39 (2019) 1230–1236

Contents lists available at ScienceDirect

Journal of the European Ceramic Society

journal homepage: www.elsevier.com/locate/jeurceramsoc

Original Article

Densification of thermodynamically unstable tin monoxide using cold sintering process

Sun Hwi Bang[*], Thomas Herisson De Beauvoir, Clive A. Randall

Materials Research Institute and Department of Materials Science and Engineering, The Pennsylvania State University, University Park, PA, 16802, USA

ARTICLE INFO

Keywords:
Cold sintering process
Tin monoxide
Low temperature processing densification
Metastable material
Thermoelectric

ABSTRACT

SnO is a thermodynamically unstable phase and undergoes thermal decomposition into SnO_2 and Sn at a relatively low temperature when heating under ambient conditions. With the cold sintering process (CSP), SnO can be densified up to 89% of theoretical density within 100 min by applying uniaxial pressure of 350 MPa and transient liquid phase. 15-fold BET specific surface area reduction is observed between the ball-milled powder and the cold-sintered pellet, indicating experimental evidence of sintering. The temperature profiles of 70–265 °C show densification while maintaining the phase purity. Water and 2 M acetic acid solution are studied as transient liquid phases which promotes dissolution-precipitation on the particle surface and induces crystalline texture. Electrical properties of the cold sintered bulk, notably electrical conductivity and Seebeck coefficient, are measured as a function of temperature.

1. Introduction

Among the Sn—O metal oxide systems, SnO (stannous oxide) is a p-type metal oxide semiconductor material with a wide optical band gap of 2.5–3.0 eV [1,2]. Also known as tin protoxide, SnO is a black colored powder soluble in acids and strong bases [3]. SnO began to receive increasing attention over the last decade for its relatively high Hall mobility and its nontoxic nature [4] and the target application has focused on gas sensors [5], thin film transistors [6–8], transparent conducting oxides [9], and anode material [10]. Furthermore, in a recent high-throughput study of bulk, polycrystalline SnO is regarded as a potential p-type thermoelectric material [11].

Although it shows promising material properties and applications, SnO still remains highly challenging to process, due to its very low phase transformation temperature between 240–420 °C. During the thermal decomposition reaction, SnO forms an intermediary phase of Sn_3O_4, then further decomposes into SnO_2 and Sn regardless of oxygen atmosphere [12–15]. For this reason, it has been difficult to process SnO while maintaining phase purity. As the temperature of conventional solid-state sintering of metal oxide is usually above 1000 °C, the conventional method is not a feasible option for sintering thermodynamically unstable materials that decompose into other phases at low temperature.

Reducing sintering temperature not only allows the ability to densify ceramic materials of low thermal decomposition temperature without the secondary phase evolution but also offers multiple advantages such as energy efficient manufacturing process [16], device miniaturization [17], integration between ceramic/polymer materials [18,19], and novel physical properties of nanocrystalline material [20,21]. The recent studies on ultra-low temperature sintering include solid state reaction of $NaAgMoO_4$ at 400 °C [22], spark plasma sintering of thermodynamically unstable compounds (carbonates, sulfates, and phosphates) at 400 °C [23], hydrothermal sintering of nanosized α-quartz at 300 °C [24], and cold sintering of $LiFePO_4$-based cathode composite at 240 °C [25].

The objective of this work is to study the possibility of using to use the cold sintering process (CSP) to stabilize and densify thermodynamically unstable material system that undergoes decomposition relatively low temperature. The CSP has now been recognized as a process methodology to densify ceramics below 300 °C within a few minutes by employing a transient liquid phase to mediate the dissolution-precipitation process under a uniaxial pressure, which allows integration of ceramic oxide and polymer composite [18,19,26–28]. Due to its ultra-low processing temperature, tape casting and screen printing techniques enable fabrication of ceramic/polymer multilayer device and printable electronics [29,30].

---

[*] Corresponding author.
E-mail address: sxb575@psu.edu (S.H. Bang).

https://doi.org/10.1016/j.jeurceramsoc.2018.11.026
Received 7 August 2018; Received in revised form 11 November 2018; Accepted 15 November 2018

2. Experimental

2.1. Powder preparation

The initial SnO powder was purchased from a commercial supplier, Alfa Aesar (99.9%). To reduce the powder agglomerate size, the weight ratio of the 1 SnO powder and 5 alumina grinding beads was mixed by a vibratory ball milling for 24 h with ethanol followed by overnight drying at 80 °C. After the beads were removed, the dried powder was then ground using a pestle and mortar to shear any lumps formed during the previous ethanol drying process. Note that the initial powder was also used in this study to determine the particle size effects on density, microstructure, and thermoelectric properties.

2.2. Cold sintering process

1.0 g of the SnO powder was mixed with 15 wt.% of deionized water or 2 M acetic acid solution (pH = 2.23). In order to disperse the added transient liquid over the whole powder, the powder and liquid were manually ground in an agate mortar for 5 min. The mixture was then poured into 12.7 mm diameter stainless steel die. Two 0.127 mm thick polyimide films were placed on the top and bottom of the powder layer to minimize any uneven pressure distribution and contamination from the punch surfaces. The sintering die was uniaxially pressed at 350 MPa and heated using a manual hydraulic press with dual heating plates (Carver 4386) and the internal temperature profile was monitored via a thermocouple placed on the middle punch (Fig. 1a*)*. The sintering temperature ranged from 70 to 265 °C with the maximum heating ramp of 5.4 °C/minute (Fig. 1b*)* and the dwell time was 45 min at the steady state temperature. During the cooling, the uniaxial pressure was released and fan-cooled down to room temperature.

2.3. Material characterizations

The skeletal density of both ball-milled powder and cold-sintered pellet was measured by He gas pycnometer (Micromeritics Accupyc II 1340). The envelope density ($m_d/V_{envelope}$) was quantified by the Archimedes method using acetone as the liquid medium at ambient temperature. The mass of the dry pellet (m_d) was first measured. Then the sample was immersed in acetone for 5 min to completely fill open pores with the fluid. After the sample surface was gently wiped to remove any excess on the surface, the mass of the sample saturated with liquid (m_s) was measured in air and the mass of the sample suspended in liquid (m_l) was measured in the liquid medium. The envelope volume was calculated by the following relation:

$$V_{envelope} = \frac{(m_s - m_l)}{\rho_{fluid}} \tag{1}$$

The particle sizes of the initial and ball-milled powder were measured by laser particle size analyzer (Malvern Mastersizer 3000). The thermal decomposition temperature was determined by thermogravimetric analysis (TA Instrument TGA Q5500) operated at the heating ramp of 5 °C/min in air atmosphere. The BET surface area measurements of the ball-milled powder and the cold-sintered pellet were obtained by N_2 gas molecule adsorption after the sample degassing at 80 °C for 8 h (ASAP 2020 Automated Surface Area and Porosimetry System). The microstructures of the iridium-sputtered powder and the fractured surfaces were imaged by scanning electron microscope (FEI Nova NanoSEM 630) performed at the landing energy of 5 keV. X-ray diffraction (PANalytical Empyrean) characterized phase purity and preferred orientation. The disk-like pellets were cut and polished into a rectangle to have exact geometry appropriate for the four-point probe Seebeck coefficient and electrical conductivity measurement (Linseis LSR-3). The electrode was 100 nm thick sputter-coated Ag (Quorum Q150R).

3. Results and discussion

3.1. Effects of vibratory ball milling on SnO powder

The laser particle size analyzer characterized the sizes of the initial agglomerate the ball-milled powder (Fig. 2a). The SnO commercial powder has unimodal size distribution at 20 μm and the microstructure shows agglomerates of 2.5 μm long platelets (Fig. 3a). After 24-hour vibratory ball milling, these agglomerates were broken resulting in a bimodal size distribution with the major population centered at 0.05 μm and the minor one at 1 μm. The microstructure of the ball-milled powder indicates that particles are no longer platelets but irregularly shaped (Fig. 3c*)*. The thermal decomposition temperature was also significantly impacted by the ball-milling process and the particle size (*Figure 2b*) and the weight increase indicates the oxidation process of SnO. The initial SnO powder undergoes thermal decomposition at 500 °C whereas the ball-milled powder begins to oxide at 200 °C. Although the phase transition temperature of the initial SnO is in agreement with the reported values [14], the ball-milled powder shows 40 °C lower than the lowest temperature reported [13]. Ethanol-based vibratory ball-milling or resulting particle size reduction may shift the stable temperature range of SnO from 500 °C to 200 °C. The ball-milling of the agglomerated SnO powder effectively reduces the particle size distribution from 20 μm to 1 μm but also increases thermal instability, adding the challenge of densification and phase stability.

3.2. Effects of particle size and transient liquid on SnO cold sintering process

For the SnO cold sintering process (CSP), two different particle sizes (initial powder and ball-milled powder) and transient liquid phases (deionized water and 2 M acetic acid) were studied. Examining the effects of particle size allows understanding of how particle arrangement and surface area would affect a densification process. As the CSP is

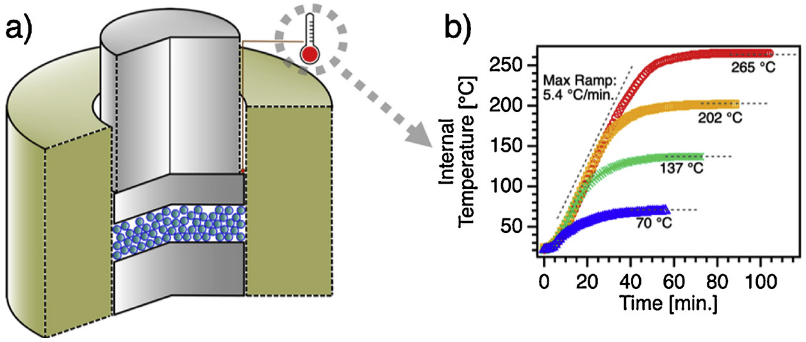

Fig. 1. (a) Schematic diagram of the cold sintering process with internal die temperature measurements (b) sintering temperature profiles of 70, 137, 202, and 265 °C with 45-minute dwell time.

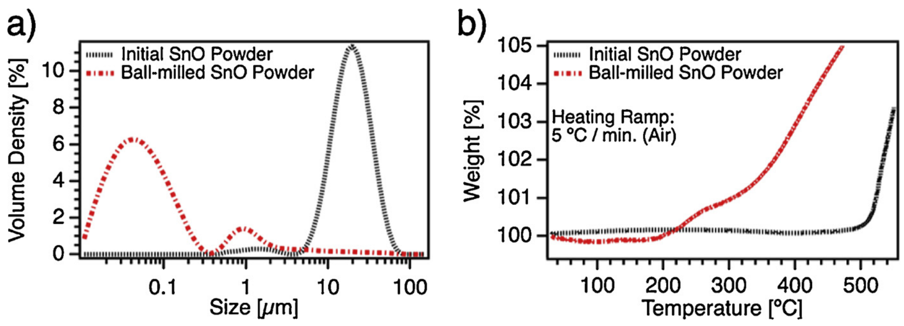

Fig. 2. Effects of 24-hour vibratory ball-milling on (a) laser particle size analyzer and (b) TGA under air.

driven by dissolution – precipitation process [18,25,31], using acetic acid would promote more dissolutions on the particle surface compared to deionized water, resulting a higher mass gradient at the solid – liquid interface. Applying heat would increase the solubility of SnO in the transient liquid phase, and the uniaxial pressure helps the particle rearrangement and would also enhance the mass transport between the dissolution and precipitation sites.

For the initial powder CSP with acetic acid, the columnar grain growth was observed (Fig. 3b) and each platelet of the agglomerate elongated from 2.5 μm up to 50 μm after the CSP. Considering that the SnO CSP takes place within 100 min, such radical SnO grain growth pertains to its thermodynamically unstable nature [15]. For the ball-milled CSP with acetic acid, the starting particle size of 0.05 μm formed the grains of 1.5 μm after the sintering (Fig. 3d*)*. For both initial and ball-milled CSP cases, significant grain size growth was observed. Understanding such fast grain growth mechanism is still in progress but the dissolution – precipitation plays a key role in the CSP. Therefore, identifying its mass-transport process would be a next step, which will be discussed in the next section.

The evolution of pellet relative densities at different sintering temperatures (70–265 °C) is presented in Fig. 4. The relative density is formulated by dividing envelope density over theoretical density. For both particle sizes and transient liquid phases, the densities increase as the sintering temperature increases. In the case of the initial powder, the maximum density was 84% whereas the ball-milled powder was densified up to 89% of the theoretical density. Such density enhancement can be related to increased surface and improved interparticle packing due to the particle size reduction. Moreover, the smaller particles have more energetically active surface, thus enhancing dissolution at the particle-liquid interfaces, therefore filling the pores by precipitation, which leads to higher densification.

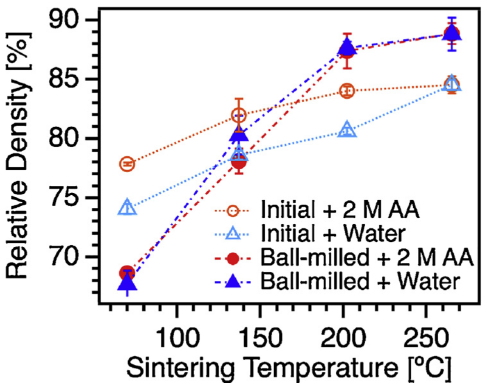

Fig. 4. Relative density vs. sintering temperature of different particle sizes (20 μm and 0.05 μm) and transient liquids (deionized water and 2 M acetic acid solution).

Selecting an appropriate transient liquid phase is critical to enabling the dissolution-precipitation process for the CSP of a given material system. However, for the SnO CSP, understanding the effects of different transient liquid phases is somewhat indeterminate. In the initial powder case, using acetic acid increases the relative density up to 4% compared to deionized water at the sintering temperature below 200 °C, but both liquids reach the density within the measurement uncertainty at 265 °C. This may indicate that acetic acid effectively induces activation energy reduction for the densification process at low

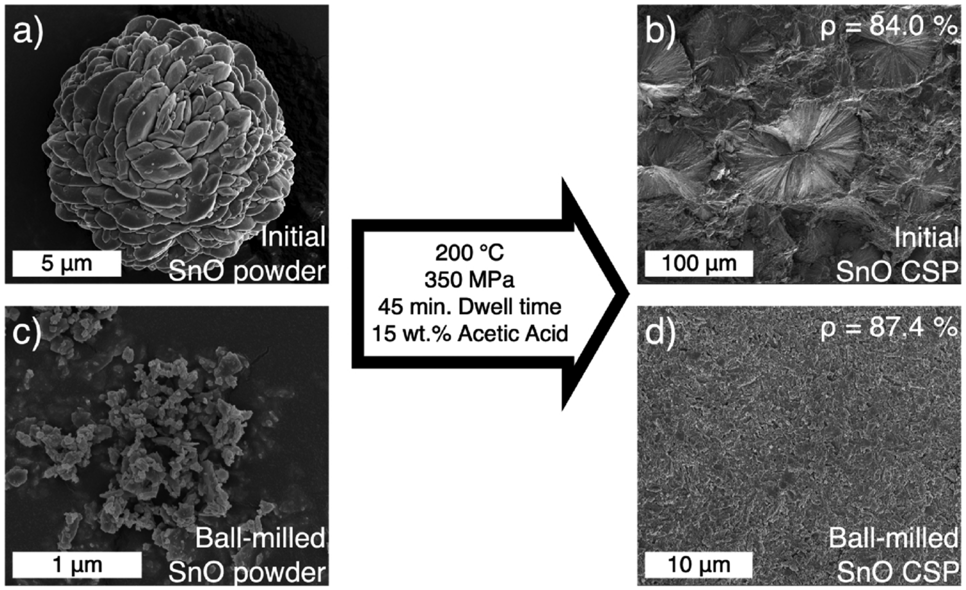

Fig. 3. SEM micrographs of a) initial SnO agglomerate, and b) fractured pellet of the initial SnO powder cold sintered at 202 °C, uniaxially pressed by 350 MPa with 15 wt.% of 2 M acetic acid. c) 24 h vibratory ball milled SnO powder, and d) fractured pellet of the ball-milled SnO powder cold sintered with the same condition of b). For the fracture pellet images, the pressing direction is parallel with the images.

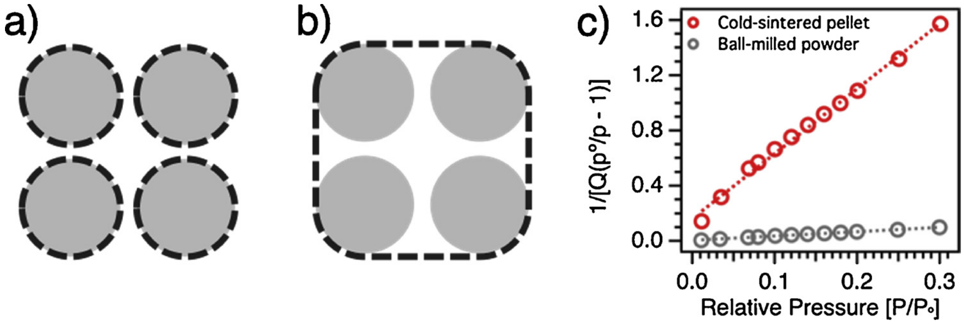

Fig. 5. a) Representation of skeletal density, b) representation of envelope density, and c) BET specific surface area plot of the ball-milled powder and the cold-sintered pellet.

temperatures. In the ball-milled powder case, no density difference was observed for using deionized water or acetic acid as a transient liquid phase. Further investigation is needed to understand chemical-mechanical behavior of the added transient liquid under pressure and heat.

3.3. Characterization of different densities and surface area reduction by sintering

Different densities of the ball-milled powder and the cold-sintered pellet were thoroughly examined. Starting from the definitions of different density terms, theoretical density is calculated from material crystal structure and lattice parameter. By knowing the total mass of atoms in a single lattice cell and the volume of the unit cell, the theoretical density can be obtained. Skeletal density (also termed as absolute density) is determined when the volume measurement excludes the pores between particles within the bulk sample (Fig. 5a), whereas, envelope density (also labelled as bulk density) is obtained when the volume measurement includes open pore spaces (Fig. 5b).

The skeletal density of the ball-milled powder and the cold-sintered pellet was measured using He gas pycnometer (Table 1). The samples were dried at 80 °C overnight to remove any ambient moisture. Comparing the theoretical density and the skeletal density of the SnO powder, the skeletal density was lower by 4.65% which could be due to the powder defects including remainder of particle aggregation after the ball-milling, absorption of ambient water, and presence of other impurities. The skeletal density of the pellet also had lower density by 2.95% indicating possible formation of a secondary or amorphous phase, evolution of a closed porosity, or residue of a transient liquid phase. Considering the low sintering temperature and the short processing time of the CSP, the resulting sample may have residual organic species including Tin(II) acetate and hydroxyl groups. Although the relative density is often formulated by dividing the envelope density over the theoretical density, the He gas pycnometer measurements have shown that relative density can be noticeably changed based on the skeletal densities and such change is 5-fold larger than the errors associated with the given relative density. Therefore, it is important to verify the skeletal density of the powder and the pellet to rigorously investigate the relative density measurement.

Along with the different density measurements, the N_2 physisorption isotherm measurement also adds an interesting aspect on the SnO cold sintering process. Note that the sintering is defined as a processing technique that uses thermal energy to enhance mechanical strength and to reduce surface area, which often results densification [32]. Combining the definition of sintering and the Brunauer, Emmett, and Teller (BET) theory, the surface area reduction between the ball-milled powder and the cold-sintered sample provides unambiguous evidence of the SnO sintering. A similar experimental approach has been studied on silica hydrothermal sintering [33]. The effectiveness of the BET theory is to obtain experimental calculation of the number of molecules needed to form a monolayer on surface, and the relation between weight adsorbed (Q) and the relative pressure ($P/P_\circ$) is denoted as [34]:

$$\frac{1}{Q\left(\frac{P_\circ}{P}-1\right)}=\frac{C-1}{Q_mC}\left(\frac{P}{P_\circ}\right)+\frac{1}{Q_mC} \tag{2}$$

where the slope of BET surface area plot corresponds to $(C-1)/(Q_mC)$ and the y-intercept is $1/(Q_mC)$. The specific surface area (S_t/w) can be determined once the weight adsorbed in a completed monolayer (Q_m) is determined:

$$\frac{S_t}{w}=\frac{Q_mN_AA_M}{M} \tag{3}$$

where N_A is Avogadro's number, A_M is molecular cross-sectional area, and M is molecular weight of N_2.

The BET specific surface areas of the ball-milled powder and the cold-sintered pellet are 13.47 m^2/g and 0.89 m^2/g, respectively (Fig. 5c). The 15-fold specific surface area reduction refers to significant decreases of the weight of N_2 adsorption which indicates the interparticle neck formation and pore area reduction during the CSP. Although the BET theory is based on the arrangement of exactly one monomolecular layer on the surface, but such uniform monolayer does not exist in the case of physisorption. However, in the low relative pressure region of $P/P_\circ = 0.05 - 0.3$, near completed monolayers enable covering of the surface and the BET theory and experimental isotherm are in agreement, leading to highly informative method of surface area determination [35]. For this CSP study, the BET technique was first introduced to show substantial surface area reduction between the powder and the sintered pellet, but such a method will also allow further identification of the mass-transport process via the kinetics of the specific surface area reduction [36].

Table 1
Summary of different density characteristics and BET surface area of the ball-milled powder and cold-sintered pellet.

	Ball-milled SnO powder	Cold-sintered SnO pellet
Sintering temperature [°C]	N/A	164
Theoretical density [g/cm^3]	6.45	N/A
Skeletal density [g/cm^3]	6.15 ± 0.009	6.26 ± 0.014
Envelope density [g/cm^3]	N/A	5.47 ± 0.057
Relative density [%]	N/A	84.81 ± 0.883
Specific surface area [m^2/g]	13.47 ± 0.131	0.89 ± 0.021

3.4. Phase stability

X-ray diffraction (XRD) was performed on the cold-sintered pellets of the different sintering temperatures (70–265 °C) and transient liquid phases to study the phase stability after the CSP (Fig. 6). No secondary phase was observed for the initial powder case regardless of the sintering temperature. However, in the ball-milled powder case, additional peak was found at 2θ = 26.63°, corresponding to SnO_2 (110). The

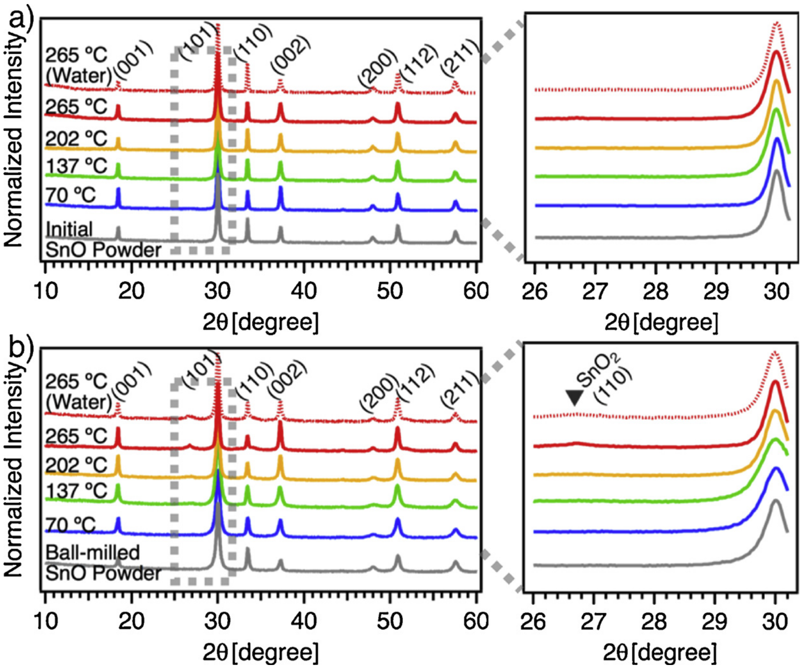

Fig. 6. XRD patterns of (a) initial SnO powder and cold sintered pellets at different sintering temperatures with acetic acid and water, and (b) ball-milled SnO powder and cold sintered pellets. The zoomed views show the presence of SnO_2 phase.

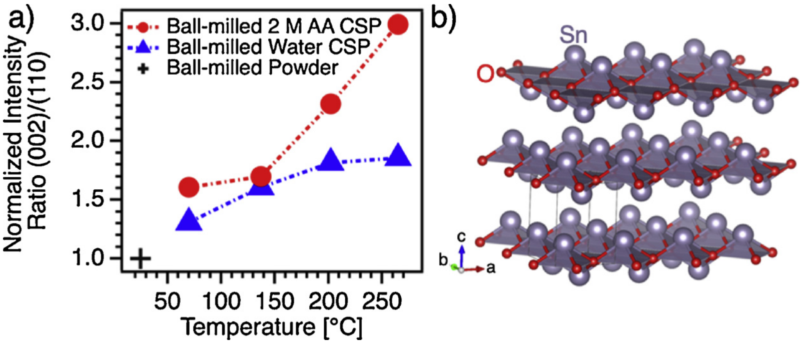

Fig. 7. (a) Normalized XRD intensity ratio of (002)/(110) peaks of milled SnO CSP samples at different sintering temperature and (b) crystal structure of SnO (P4/nmm).

presence of SnO_2 indicates that the phase stability is no longer maintained above 200 °C for the small particle size. These observations are consistent with the phase transition temperature measured in TGA. Therefore, reducing sintering temperature must be considered for sintering smaller SnO particles.

Adding a transient liquid phase is intended to promote dissolution at the solid – liquid interface but it also induces crystalline texture. Fig. 7*a* shows the normalized peak intensity ratio of (002)/(110) of the ball-milled powder CSP with deionized water and acetic acid. The ratio is normalized to that peak intensity of the ball-milled powder. For both liquid phases, the normalized peak intensity ratio increases along with the sintering temperature, but such crystal anisotropy is highly enhanced in the acetic acid case. This shows that anisotropy is induced during the CSP, which could be related to effects of liquid phase, pressure, or heat. The observation of inducing anisotropy based on the presence of liquid phase can be an opportunity to control the degree of crystalline texture for tuning bulk properties. The anisotropic peak intensity ratio of (002)/(110) is also reported in the SnO nano-rectangle strips [37], which also supports its platelet growth behavior.

3.5. *Thermoelectric characterizations*

Bulk thermoelectric properties including Seebeck coefficient and electrical conductivity are characterized over a temperature range of 50 °C–200 °C (Fig. 8). The maximum temperature was determined by the sintering temperature to prevent any undesired thermal treatment on a cold-sintere pellet. For this study, acetic acid was used for both initial powder and ball-milled powder CSP to compare the particle size effects on the thermoelectric properties. For both cases, positive values of the Seebeck coefficient indicate the p-type nature of SnO, which is related to an electronic compensation of Sn vacancies. Compared to the high-throughput calculations of bulk SnO [11], the Seebeck coefficients of the initial powder CSP and the ball-milled powder CSP are 88% and 92% of the prediction at 200 °C. The electrical conductivities are 48% and 10% of the prediction at 200 °C, respectively. The significant difference on the electrical conductivities could be related to several causes, including remaining porosity acting like an insulator and residue of acetate phase or amorphous phase. By utilizing low processing temperature, conductive polymer such as PEDOT:PSS can be used to design grain boundaries to enhance properties for practical applications, as recently shown by Zhao et al. [38].

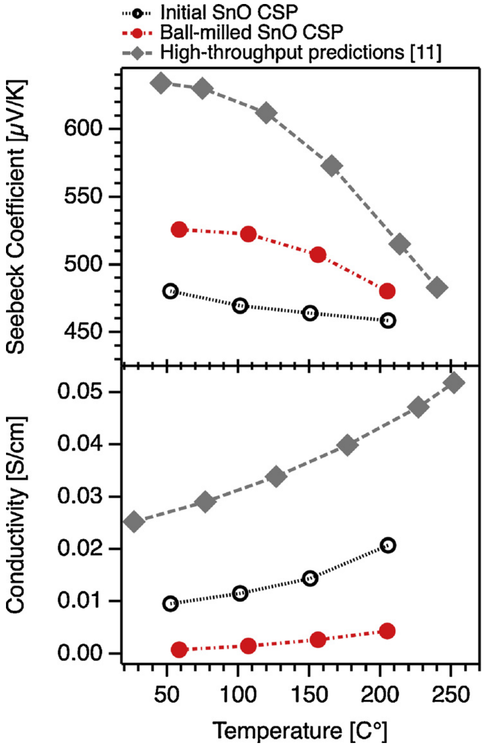

Fig. 8. Seebeck coefficient and electrical conductivity measurement of initial and ball-milled SnO powder CSP samples sintered at 202 °C with acetic acid.

4. Conclusions

Sintering SnO involves a key challenge to densify before the low temperature phase decomposition reactions. The cold sintering process (CSP) of SnO showed that the thermodynamically unstable material can be densified without inducing its thermal decomposition into SnO_2 and Sn. By applying uniaxial pressure and heat, the initial SnO powder was sintered without the formation of secondary phases. However, for the ball-milled SnO powder, both XRD and TGA indicated the presence of SnO_2 above 200 °C. Reducing the particle size led to densification up to 89% of theoretical density within 100 min. The skeletal density measured by He gas pycnometer shows that the density difference between the experimental and the theoretical could result up to 4.65%. The BET measurement showed a 15-fold decrease in the specific surface area between the powder and pellet, which could be due to interparticle neck formation and pore area reduction by the sintering process. Using acetic acid as a transient liquid phase resulted in radical columnar grain growth and enhanced the crystalline texture. The characterizations of Seebeck coefficient and electrical conductivity verified p-type nature of SnO. These results indicate that CSP opens up new opportunities for property exploration in thermodynamically unstable materials and development of functional composites sintered at heavily reduced temperature and time.

Acknowledgements

We gratefully acknowledge support from National Science Foundation (DMR-1728634). We also wish to thank Dr. Arnaud Ndayishimiye for density measurement discussion and Materials Characterization Lab at the Pennsylvania State University for the characterization guidance.

References

[1] Y. Ogo, H. Hiramatsu, K. Nomura, H. Yanagi, T. Kamiya, M. Hirano, H. Hosono, p-channel thin-film transistor using p-type oxide semiconductor, SnO, Appl. Phys. Lett. 93 (2008) 032113, https://doi.org/10.1063/1.2964197.

[2] J. Geurts, S. Rau, W. Richter, F.J. Schmitte, SnO films and their oxidation to SnO2: raman scattering, IR reflectivity and X-ray diffraction studies, Thin Solid Films 121 (1984) 217–225, https://doi.org/10.1016/0040-6090(84)90303-1.

[3] H.A. Ávila, J.E. Rodríguez-Páez, Solvent effects in the synthesis process of tin oxide, J. Non. Solids 355 (2009) 885–890, https://doi.org/10.1016/j.jnoncrysol.2009.03.004.

[4] J.F. Wager, B. Yeh, R.L. Hoffman, D.A. Keszler, An amorphous oxide semiconductor thin-film transistor route to oxide electronics, Curr. Opin. Solid State Mater. Sci. 18 (2014) 53–61, https://doi.org/10.1016/j.cossms.2013.07.002.

[5] V.X. Hien, J.H. Lee, J.J. Kim, Y.W. Heo, Structure and NH_3 sensing properties of SnO thin film deposited by RF magnetron sputtering, Sensors Actuators, B Chem. 194 (2014) 134–141, https://doi.org/10.1016/j.snb.2013.12.086.

[6] K. Okamura, B. Nasr, R.A. Brand, H. Hahn, Solution-processed oxide semiconductor SnO in p-channel thin-film transistors, J. Mater. Chem. 22 (2012) 4607, https://doi.org/10.1039/c2jm16426d.

[7] Y. Ogo, H. Hiramatsu, K. Nomura, H. Yanagi, T. Kamiya, M. Kimura, M. Hirano, H. Hosono, Tin monoxide as an s-orbital-based p-type oxide semiconductor: electronic structures and TFT application, Phys. Status Solidi Appl. Mater. Sci. 206 (2009) 2187–2191, https://doi.org/10.1002/pssa.200881792.

[8] H.N. Lee, H.J. Kim, C.K. Kim, p-Channel Tin Monoxide Thin Film Transistor Fabricated by Vacuum Thermal Evaporation, (2010), https://doi.org/10.1143/JJAP.49.020202.

[9] L.Y. Liang, Z.M. Liu, H.T. Cao, X.Q. Pan, Microstructural, Optical, and Electrical Properties of SnO Thin Films Prepared on Quartz via a Two-Step Method 2 (2010), pp. 2–7, https://doi.org/10.1021/am900838z.

[10] H. Yamaguchi, S. Nakanishi, H. Iba, T. Itoh, Amorphous polymeric anode materials from poly(acrylic acid) and tin(II) oxide for lithium ion batteries, J. Power Sources 275 (2015) 1–5, https://doi.org/10.1016/j.jpowsour.2014.10.071.

[11] S.A. Miller, P. Gorai, U. Aydemir, T.O. Mason, V. Stevanović, E.S. Toberer, G.J. Snyder, SnO as a potential oxide thermoelectric candidate, J. Mater. Chem. C Mater. Opt. Electron. Devices (2017) 8854–8861, https://doi.org/10.1039/C7TC01623A.

[12] F. Lawson, Tin oxide - Sn_3O_4, Nature. 215 (1967) 955, https://doi.org/10.1038/215955a0.

[13] C.G. Fink, C.L. Mantell, Some physico-chemical properties of stannous oxide, J. Phys. Chem. 32 (1927) 103–112, https://doi.org/10.1021/j150283a007.

[14] C.M. Campo, J.E. Rodríguez, A.E. Ramírez, Thermal behaviour of romarchite phase SnO in different atmospheres: a hypothesis about the phase transformation, Heliyon 2 (2016) 1–13. 10.1016/j.heliyon.2016.e00112.

[15] L. Brewer, The thermodynamic properties of the oxides and their vaporization processes, Chem. Rev. 52 (1953) 1–75, https://doi.org/10.1021/cr60161a001.

[16] D. Sohrabi Baba Heidary, M. Lanagan, C.A. Randall, Contrasting energy efficiency in various ceramic sintering processes, J. Eur. Ceram. Soc. 38 (2018) 1018–1029, https://doi.org/10.1016/j.jeurceramsoc.2017.10.015.

[17] M. Valant, D. Suvorov, R.C. Pullar, K. Sarma, N.M.N. Alford, A mechanism for low-temperature sintering, J. Eur. Ceram. Soc. 26 (2006) 2777–2783, https://doi.org/10.1016/j.jeurceramsoc.2005.06.026.

[18] J. Guo, H. Guo, A.L. Baker, M.T. Lanagan, E.R. Kupp, G.L. Messing, C.A. Randall, Cold sintering: a paradigm shift for processing and integration of ceramics, Angew. Chemie - Int. Ed. 55 (2016) 11457–11461, https://doi.org/10.1002/anie.201605443.

[19] J. Guo, H. Guo, D.S.B. Heidary, S. Funahashi, C.A. Randall, Semiconducting properties of cold sintered V_2O_5ceramics and Co-sintered V2O5-PEDOT:PSS composites, J. Eur. Ceram. Soc. 37 (2017) 1529–1534, https://doi.org/10.1016/j.jeurceramsoc.2016.11.021.

[20] C. Bousquet, C. Elissalde, C. Aymonier, M. Maglione, F. Cansell, J.M. Heintz, Tuning Al2O3crystallinity under supercritical fluid conditions: effect on sintering, J. Eur. Ceram. Soc. 28 (2008) 223–228, https://doi.org/10.1016/j.jeurceramsoc.2007.06.005.

[21] I.-W. Chen, X.-H. Wang, Sintering dense nanocrystalline ceramics without final-stage grain growth, Nature. 404 (2000) 168, https://doi.org/10.1038/35004548.

[22] Z. Di, P. Li-Xia, Q. Ze-Ming, J. Biao-Bing, Y. Xi, Novel ultra-low temperature co-fired microwave dielectric ceramic at 400 degrees and its chemical compatibility with base metal, Sci. Rep. 4 (2014) 5–8, https://doi.org/10.1038/srep05980.

[23] T. Herisson De Beauvoir, A. Sangregorio, I. Cornu, C. Elissalde, M. Josse, Cool-SPS: an opportunity for low temperature sintering of thermodynamically fragile materials, J. Mater. Chem. C Mater. Opt. Electron. Devices 6 (2018) 2229–2233, https://doi.org/10.1039/c7tc05640k.

[24] A. Ndayishimiye, A. Largeteau, M. Prakasam, S. Pechev, M.A. Dourges, G. Goglio, Low temperature hydrothermal sintering process for the quasi-complete densification of nanometric α-quartz, Scr. Mater. 145 (2018) 118–121, https://doi.org/10.1016/j.scriptamat.2017.10.023.

[25] J.H. Seo, J. Guo, H. Guo, K. Verlinde, D.S.B. Heidary, R. Rajagopalan, C.A. Randall, Cold sintering of a Li-ion cathode: LiFePO4-composite with high volumetric capacity, Ceram. Int. 43 (2017) 15370–15374, https://doi.org/10.1016/j.ceramint.2017.08.077.

[26] J. Guo, S.S. Berbano, H. Guo, A.L. Baker, M.T. Lanagan, C.A. Randall, Cold sintering process of composites: bridging the processing temperature gap of ceramic and polymer materials, Adv. Funct. Mater. 26 (2016) 7115–7121, https://doi.org/10.1002/adfm.201602489.

[27] X. Zhao, J. Guo, K. Wang, T. Herisson De Beauvoir, B. Li, C.A. Randall, Introducing a ZnO-PTFE (Polymer) nanocomposite varistor via the cold sintering process, Adv. Eng. Mater. 1700902 (2018) 1–8, https://doi.org/10.1002/adem.201700902.

[28] I.J. Induja, M.T. Sebastian, Microwave dielectric properties of mineral sillimanite obtained by conventional and cold sintering process, J. Eur. Ceram. Soc. 37 (2017)

2143–2147, https://doi.org/10.1016/j.jeurceramsoc.2017.01.007.

[29] A. Baker, H. Guo, J. Guo, C. Randall, Utilizing the cold sintering process for flexible–Printable electroceramic device fabrication, J. Am. Ceram. Soc. 99 (2016) 3202–3204, https://doi.org/10.1111/jace.14467.

[30] J. Guo, A.L. Baker, H. Guo, M. Lanagan, C.A. Randall, Cold sintering process: a new era for ceramic packaging and microwave device development, J. Am. Ceram. Soc. 100 (2017) 669–677, https://doi.org/10.1111/jace.14603.

[31] S. Funahashi, J. Guo, H. Guo, K. Wang, A.L. Baker, K. Shiratsuyu, C.A. Randall, Demonstration of the cold sintering process study for the densification and grain growth of ZnO ceramics, J. Am. Ceram. Soc. 100 (2017) 546–553, https://doi.org/10.1111/jace.14617.

[32] C. Greskovich, K.W. Lay, Grain growth in very porous Al2O3 compacts, J. Am. Ceram. Soc. 55 (1972) 142–146, https://doi.org/10.1111/j.1151-2916.1972.tb11238.x.

[33] A. Ndayishimiye, A. Largeteau, S. Mornet, M. Duttine, M.A. Dourges, D. Denux, M. Verdier, M. Gouné, T. Hérisson de Beauvoir, C. Elissalde, G. Goglio, Hydrothermal sintering for densification of silica. Evidence for the role of water, J. Eur. Ceram. Soc. 38 (2018) 1860–1870, https://doi.org/10.1016/j.jeurceramsoc.2017.10.011.

[34] S. Brunauer, P.H. Emmett, E. Teller, Adsorption of gases in multimolecular layers, J. Am. Chem. Soc. 60 (1938) 309–319, https://doi.org/10.1021/ja01269a023.

[35] S. Lowell, Introduction to Powder Surface Area, Jone Wiley & Sons, New York, NY, 1979.

[36] R.M. German, Z.A. Munir, Surface area reduction during isothermal sintering, J. Am. Ceram. Soc. 59 (1976) 379–383, https://doi.org/10.1111/j.1151-2916.1976.tb09500.x.

[37] M.Z. Iqbal, F. Wang, Q.Javed Rafi-ud-din, M.Y. Rafique, Y. Li, P. Li, Preparation, characterization and optical properties of tin monoxide micro-nano structure via hydrothermal synthesis, Mater. Lett. 68 (2012) 409–412, https://doi.org/10.1016/j.matlet.2011.11.023.

[38] Y. Zhao, S.S. Berbano, L. Gao, K. Wang, J. Guo, K. Tsuji, J. Wang, C.A. Randall, Cold-sintered V2O5-PEDOT:PSS nanocomposites for negative temperature coefficient materials, J. Eur. Ceram. Soc. (2018), https://doi.org/10.1016/j.jeurceramsoc.2018.10.018.